Spectral proper orthogonal decomposition and resolvent analysis of near-wall coherent structures in turbulent pipe flows

Leandra I. Abreu[1,2,†], **André V. G. Cavalieri**[2], **Philipp Schlatter**[3], **Ricardo Vinuesa**[3] **and Dan S. Henningson**[3]

[1]São Paulo State University (UNESP), Campus of São João da Boa Vista, 13876-750 SP, Brazil

[2]Divisão de Engenharia Aeronáutica, Instituto Tecnológico de Aeronáutica, São José dos Campos, 12228-900 SP, Brazil

[3]KTH Mechanics, Linné FLOW Centre, Stockholm SE-100-44, Sweden

Direct numerical simulations, performed with a high-order spectral-element method, are used to study coherent structures in turbulent pipe flow at friction Reynolds numbers $Re_\tau = 180$ and 550. The database was analysed using spectral proper orthogonal decomposition (SPOD) to identify energetically dominant coherent structures, most of which turn out to be streaks and quasi-streamwise vortices. To understand how such structures can be modelled, the linear flow responses to harmonic forcing were computed using the singular value decomposition of the resolvent operator, using the mean field as a base flow. The SPOD and resolvent analysis were calculated for several combinations of frequencies and wavenumbers, allowing the mapping out of similarities between SPOD modes and optimal responses for a wide range of relevant scales in turbulent pipe flows. In order to explore physical reasons behind the agreement between both methods, an indicator of lift-up mechanism in the resolvent analysis was introduced, activated when optimal forcing is dominated by the wall-normal and azimuthal components, and associated response corresponds to streaks of streamwise velocity. Good agreement between leading SPOD and resolvent modes is observed in a large region of parameter space. In this region, a significant gain separation is found in resolvent analysis, which may be attributed to the strong amplification associated with the lift-up mechanism, here understood as nonlinear forcing terms leading to the appearance of streamwise vortices, which in turn form high-amplitude streaks. For both Reynolds numbers, the observed concordances were generally for structures with large energy in the buffer layer. The results highlight resolvent analysis as a pertinent reduced-order model for coherent structures in wall-bounded turbulence, particularly for streamwise elongated structures corresponding to near-wall streamwise vortices and streaks.

Key words: pipe flow boundary layer, turbulent boundary layers

1. Introduction

In turbulent wall-bounded flows, such as straight pipes, channels and boundary layers, the most typically observed coherent structures are near-wall streaks, which are elongated

† Email address for correspondence: leandra.abreu@unesp.br

structures in the streamwise direction. The near-wall streaks have shown to be extremely relevant for sustaining wall-bounded turbulence (Kline *et al.* 1967; Gupta, Laufer & Kaplan 1971; Hamilton, Kim & Waleffe 1995). Such structures have regions of alternating low and high momentum located in the viscous and buffer layers with a characteristic spanwise spacing of approximately $100\nu/u_\tau$, where u_τ is the friction velocity and ν is the kinematic viscosity of the fluid (Kline *et al.* 1967; Smith & Metzler 1983; Marusic, Baars & Hutchins 2017). For higher wall-normal positions, in the logarithmic layer, larger structures are observed, with similar streaky shape, i.e. also elongated structures in the streamwise direction (Hutchins & Marusic 2007). For low and moderate Reynolds numbers, most of the turbulent production of a wall-bounded turbulent flow is located in the region close to the wall. In turn, for large Reynolds numbers, the turbulent production and dissipation contribution from the logarithmic layer could be as significant as the one from the buffer layer (Jiménez 2018). In any case, the hunt for more effective methods to model and characterize near-wall coherent structures is a very relevant problem for efficient modelling in the industry, and for a better understanding of wall-bounded turbulence dynamics.

For that matter, the use of statistical methods in flow databases can be convenient to identify coherent structures present in turbulent flow. A useful data-driven approach is proper orthogonal decomposition (POD), first introduced in the context of turbulence by Lumley (1967, 1970). Proper orthogonal decomposition consists of finding among a zero-mean stochastic process, given by an ensemble of realizations of the flow field, a number of orthonormal basis functions, called POD modes, that maximize the mean square energy. The extension of POD to the frequency domain is referred to as spectral proper orthogonal decomposition (SPOD), terminology introduced by Picard & Delville (2000). The SPOD method involves decomposition of the cross-spectral density tensor (CSD) and leads to orthonormal modes oscillating at a specific frequency, which optimally represent the second-order space–time flow statistics (Towne, Schmidt & Colonius 2018). Each SPOD mode thus represents a structure that develops coherently in space and time. This is a useful method to explore the flow dynamics, since the SPOD modes dissociate flow phenomena at different time scales.

A strong connection between linearized models and coherent structures has been provided by resolvent analysis, also called input/output analysis. In this context, the nonlinear terms from the Navier–Stokes equations are treated as external forcing, and the component-wise input/output approach is applied. Following early studies of forced transitional flows (Farrell & Ioannou 1993; Trefethen *et al.* 1993; Jovanović & Bamieh 2005), resolvent analysis considers flows in the frequency domain, and searches for forcings that lead to the most amplified flow responses. Such linearized responses from resolvent analysis can often be related to results of hydrodynamic stability theory, with modes corresponding to instability waves or to non-modal mechanisms such as lift-up (Jovanović & Bamieh 2005). Resolvent analysis has gained attention in the past decade for wall-bounded turbulent flows (Hwang & Cossu 2010; McKeon & Sharma 2010; McKeon, Sharma & Jacobi 2013). An important result is that if the forcing can be modelled as spatial white noise, a direct correspondence between SPOD and resolvent modes is expected (Towne *et al.* 2018). Moreover, for a flow with a dominant optimal forcing, leading to a gain much larger than that of suboptimal ones, the CSD will often be dominated by the leading response obtained in resolvent analysis (Beneddine *et al.* 2016; Cavalieri, Jordan & Lesshafft 2019). This indicates that SPOD is a pertinent signal-processing method for comparison of numerical or experimental databases with predictions from resolvent analysis.

In the present study a combined analysis of the flow, with SPOD on the one hand used to decompose turbulent fluctuations and resolvent analysis on the other hand as a theoretical framework, is explored for the case of the canonical turbulent pipe flow. The direct relation between both methods indicates a path to find a reduced-order model based on the linearized equations, where the focus is on the highest amplification between forcing and response. Considering a given base flow (usually the velocity profile averaged in time and homogeneous directions), the resolvent operator may be used to discern the dominant linear mechanisms in a turbulent flow, which facilitates analysis, and opens possibilities for flow estimation and control approaches aiming at the said mechanisms (Towne, Lozano-Durán & Yang 2020). A number of previous studies regarding turbulent pipe flows have dealt with POD without frequency decomposition (Hellström, Marusic & Smits 2016) and resolvent analysis (McKeon & Sharma 2010), but the ability of the latter to model SPOD modes has not been addressed quantitatively by a thorough comparison involving the range of relevant wavenumbers and frequencies. Thus, this is the main goal of the present paper, namely to map out the similarities of SPOD and resolvent modes for a turbulent pipe flow.

This paper is organized as follows. In § 2, the simulation database obtained by El Khoury *et al.* (2013) is briefly described. This section includes some results in terms of turbulence statistics and spectral analysis, with focus on the structures present in the near-wall region. Section 3 briefly describes the lift-up mechanism present in shear flows, which is relevant for the ensuing analysis. Section 4 proceeds with a description of the methods of SPOD and resolvent analysis, and the relationship between both approaches. A detailed comparison between SPOD and resolvent modes is presented and discussed in § 5. The paper is completed with conclusions in § 6.

2. Description of the employed database

The direct numerical simulation (DNS) database employed in this work was obtained by El Khoury *et al.* (2013). The simulations were carried out for the fully developed turbulent flow inside a smooth, circular straight pipe. The pressure-driven incompressible flow of a viscous Newtonian fluid was considered, where the governing equations are the time-dependent Navier–Stokes equations. The code used to solve these equations is Nek5000, developed by Fischer, Lottes & Kerkemeier (2008), which is a computational fluid dynamics solver based on the spectral-element method. This specific discretization method is characterized by spectral accuracy, favourable diffusion and dispersion properties and efficient parallelization.

The simulation domain consists of a circular pipe with radius R and length $25R$ with the pipe axis taken along the streamwise x-direction. In this study we consider two different Reynolds numbers, i.e. $Re_\tau = 180$ and 550, where Re_τ is the friction Reynolds number based on u_τ and R. Snapshots of the flow quantities within the whole computational domain are saved in a database, with non-dimensional time interval of $\delta t = 4$ (in terms of bulk velocity and pipe radius); a total of 205 snapshots for $Re_\tau = 180$, and $\delta t = 1$ and 260 snapshots for $Re_\tau = 550$ were considered for the present analysis. A streamwise pressure gradient drives the flow in the streamwise direction. Additional details of the numerical set-up can be found in the work by El Khoury *et al.* (2013).

The resultant database from the DNS is in the cylindrical coordinate system and the origin is located on the axis of the pipe. The flow is periodic in the streamwise direction x. The velocity vector is given by $\boldsymbol{q} = [\boldsymbol{u}, \boldsymbol{v}, \boldsymbol{w}]$ in streamwise, radial and azimuthal coordinates $[x, r, \theta]$, respectively, where r is the radial coordinate. Thus the
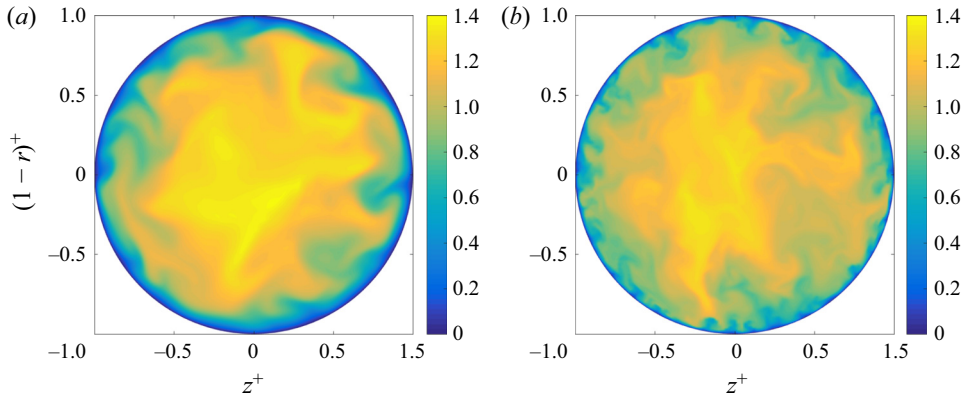
FIGURE 1. Instantaneous streamwise velocity component for both friction Reynolds numbers: (a) $Re_\tau = 180$; (b) $Re_\tau = 550$. The axis tick labels are scaled with the pipe radius.

non-dimensional wall distance can be obtained by $(1 - r)$. Figures 1(a) and 1(b) show the instantaneous streamwise velocity component u from the simulation for both $Re_\tau = 180$ and 550, respectively, where the axis tick labels are scaled with the pipe radius.

The inner velocity scaling is defined by the friction velocity u_τ, the length by the viscous length scale ν/u_τ and is denoted by the superscript $+$. In the following we will use $z^+ = r^+\theta$ as a pseudo-spanwise coordinate for simple comparison with results for planar flows such as boundary layers and channels. Thus the azimuthal wavelength λ_θ can be associated with a pseudo-spanwise wavenumber $\lambda_z^+ = r^+\lambda_\theta$. The resolvent and SPOD modes are a function of the azimuthal wavenumber m, or wavelength $\lambda_\theta = 2\pi/m$, and thus cannot be expressed as a function of a single pseudo-spanwise wavelength λ_z^+. For such modes, we define $\tilde{\lambda}_z^+ = (Re_\tau - 15)\lambda_\theta$, such that $\tilde{\lambda}_z^+$ represents the pseudo-spanwise wavelength at a reference position in the buffer layer at a distance of 15 viscous units from the wall. This allows for a comparison with similar structures found in other (planar) wall-bounded flows.

2.1. *Turbulence statistics and spectral analysis*

Using standard Reynolds decomposition $u = \bar{u} + u'$, the mean streamwise velocity profiles $\bar{u}^+$ and the variance profile of the streamwise velocity fluctuations $\bar{u}'^{2+}$ in inner scaling are shown in figures 2(a) and 2(b), respectively, for $Re_\tau = 180$ and 550. The mean velocity profiles show the expected shape of wall-bounded turbulent flows when plotted as a function of wall distance where the variable $y^+ = (1 - r)^+$ denotes the inner-scaled wall distance. Variance profiles also have the expected pattern characteristic of wall-bounded turbulent flows, with a near-wall peak in the buffer layer at $(1 - r)^+ \approx 15$, which increases its magnitude with the Reynolds number, as expected Georg, Ramis & Philipp (2014).

In order to visualize turbulent structures present in the buffer layer, figures 3(a) and 3(b) show snapshots of the streamwise velocity fluctuations (u'^+) in a wall-parallel station at $(1 - r)^+ \approx 15$, for $Re_\tau = 180$ and 550, respectively. The same analysis is shown for the logarithmic layer in figures 3(c) and 3(d) at $(1 - r)^+ \approx 100$, for $Re_\tau = 180$ and 550, respectively. These figures show that the dominant structures are elongated in the streamwise direction in all cases, with higher amplitudes near the wall in the buffer layer, in agreement with the near-wall structures found in the flow visualizations by Kline *et al.* (1967). Such long and narrow structures of the streamwise velocity component u are the well known streaks, which exhibit a range of sizes and are found between the near-wall
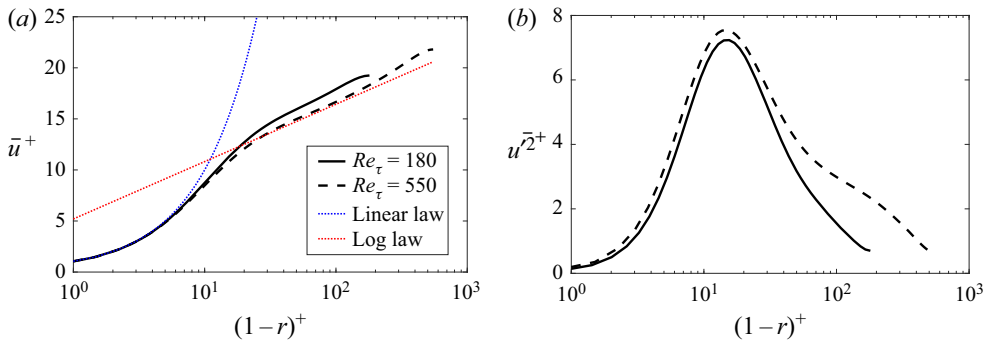
FIGURE 2. (a) The mean flow and (b) streamwise velocity fluctuations at $Re_\tau = 180$ (black solid line) and 550 (black dashed line), both scaled in viscous units. In panel (a) the blue dashed line represents the linear law, $\bar{u}^+ = (1 - r)^+$; and the red dashed line is the log law, $\bar{u}^+ = (1/\kappa) \ln(1 - r)^+ + B$, where $\kappa = 0.41$ and $B = 5.2$.
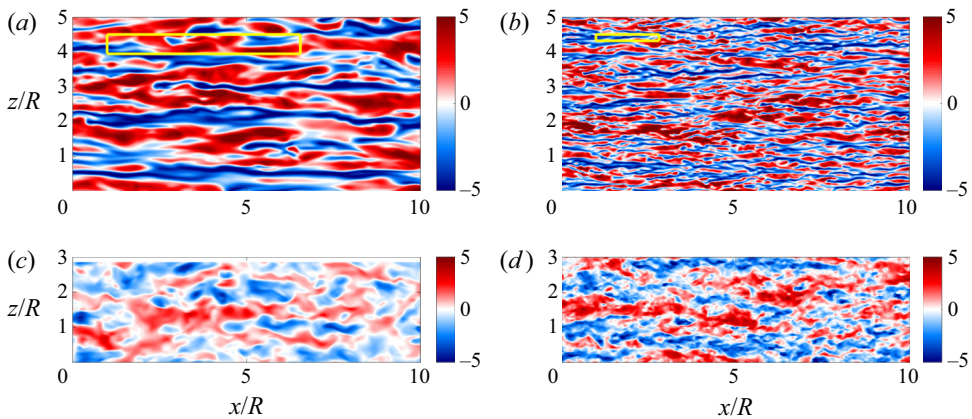

FIGURE 3. Instantaneous streamwise velocity fluctuation (u'^+) field in the wall-parallel plane for both friction Reynolds numbers, where panels (a,b) show the results in the buffer layer $(1 - r)^+ \approx 15$, and the yellow rectangle represents a box with $(\lambda_x^+, \lambda_z^+) \approx (1000, 100)$; panels (c,d) show the results in the logarithmic layer $(1 - r)^+ \approx 100$. (a) $Re_\tau = 180$ at $(1 - r)^+ \approx 15$; (b) $Re_\tau = 550$ at $(1 - r)^+ \approx 15$; (c) $Re_\tau = 180$ at $(1 - r)^+ \approx 100$; (d) $Re_\tau = 550$ at $(1 - r)^+ \approx 100$.

region and the pipe core. The near-wall streaks have an amplitude peak at $(1 - r)^+ \approx 15$, in the buffer-layer, and have a characteristic peak for the axial and azimuthal wavelengths of $(\lambda_x^+, \lambda_z^+) \approx (1000, 100)$, represented by the yellow rectangle in figures 3(a) and 3(b). In what follows we denote as streaky structures, the structures elongated in the streamwise direction, with an aspect ratio such that $\lambda_x^+ > 2\lambda_z^+$ at least. Although this is a somewhat arbitrary choice, it will focus the analysis on the dominant elongated structures visible in figure 3.

The two-dimensional inner-scaled premultiplied power-spectral density of streamwise velocity fluctuations $k_x k_z E_{uu}^+$ at $(1 - r)^+ \approx 15$ are shown in figures 4(a) and 4(b) for $Re_\tau = 180$ and 550, respectively, where k_x and k_z refer to streamwise and azimuthal wavenumbers, respectively. For both Reynolds numbers, the results in figure 4 show a highly energetic peak located in the near-wall region $(1 - r)^+ \approx 15$ for the wavelength
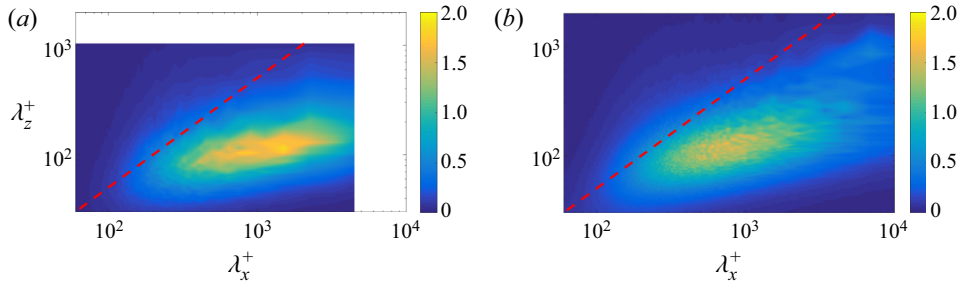
FIGURE 4. Two-dimensional inner-scaled premultiplied power-spectral density of the streamwise velocity $k_x k_z \boldsymbol{E}_{uu}^+$, at $(1-r)^+ \approx 15$, for (a) $Re_\tau = 180$ and (b) $Re_\tau = 550$. The red dashed line represents $\lambda_x^+ = 2\lambda_z^+$.

combination $(\lambda_x^+, \lambda_z^+) \approx (1000, 100)$, which is representative of the signature of the near-wall cycle of streaks and quasi-streamwise vortices, which has been discussed at length in many studies across a range of Reynolds numbers and flow types (see for instance Hoyas & Jiménez (2006), Monty *et al.* (2009) and Smits, McKeon & Marusic (2011)). Figure 4 shows that most of the fluctuation energy is related to the aforementioned streaks, since the pre-multiplied spectrum has most of its content for $\lambda_x^+ > 2\lambda_z^+$ (below the red dashed line).

The visualizations shown in figure 3 and the spectra in figure 4 indicate that the turbulent pipe flow is dominated by near-wall streaks for the Reynolds numbers considered here. In the next section we review the lift-up mechanism, which is a key aspect in the dynamics of such streaky structures.

3. The lift-up mechanism

The lift-up mechanism was introduced in the work by Ellingsen & Palm (1975), who identified a linear mechanism responsible for the amplification of fluctuations in shear flows, followed by the work by Landahl (1980). Ellingsen & Palm (1975) concluded that a finite disturbance independent of the streamwise coordinate leads to algebraic growth of disturbances in shear flows, even though the basic velocity does not possess any inflection point. The concept of lift-up effect has been recently explored in detail by Brandt (2014).

We briefly outline here the derivations of the equations highlighting the lift-up effect. We consider a parallel velocity profile as $\bar{\boldsymbol{u}} = (\bar{u}, \bar{v}, \bar{w}) = (\bar{u}(y), 0, 0)$ where the overbar denotes averaging in the homogeneous directions and time. In its simplest derivation, the lift-up effect may be explored by considering Cartesian coordinates, but similar effects are obtained in polar coordinates (Ellingsen & Palm 1975). Thus, considering this flow as inviscid and incompressible, bounded by two parallel planes, subject to disturbances independent of the streamwise coordinate x, the equation for the streamwise component of the velocity fluctuations and for the streamwise vorticity, ξ, reduce, respectively, to

$$\frac{\mathrm{D}u'}{\mathrm{D}t} = 0, \quad \frac{\mathrm{D}\xi}{\mathrm{D}t} = 0. \tag{3.1a,b}$$

Introducing the streamfunction Ψ for the cross-stream components

$$v' = \frac{\partial \Psi}{\partial z}, \quad w' = -\frac{\partial \Psi}{\partial y}, \tag{3.2a,b}$$

and upon linearization, we obtain for the streamwise component

$$\frac{\partial u'}{\partial t} + v' \frac{\mathrm{d}\bar{u}}{\mathrm{d}y} = 0, \tag{3.3}$$

and for the cross-stream flow, i.e. y and z components, we obtain

$$\frac{\partial \nabla^2 \Psi}{\partial t} = 0, \tag{3.4}$$

where ∇^2 is the two-dimensional Laplacian. We can see from (3.4) that the cross-stream velocity components are independent of time, i.e. a streamwise-independent perturbation v' will not grow or decay in an inviscid flow. Equation (3.3) can be integrated in time

$$u' = u'(0) - v' \frac{\mathrm{d}\bar{u}}{\mathrm{d}y} t \tag{3.5}$$

to show that the perturbation u' grows linearly in time, from which comes the term algebraic inviscid instability. An addition of viscous effects limits the algebraic growth in (3.5), which nonetheless may be of some orders of magnitude for higher Reynolds numbers (Brandt 2014).

The term $v' \, \mathrm{d}\bar{u}/\mathrm{d}y$ in (3.3) is responsible for the lift-up effect, and represents the deformation of the mean velocity profile by the spanwise variations of v'. This is one of the terms responsible for non-orthogonal eigenvectors of the evolution operator (Jiménez 2018). Thus, the streamwise vortices, (v', w'), lead to the formation of low- and high-momentum streaks, since lift-up acts most strongly on long narrow features. Lift-up works by moving low-velocity fluid from the wall upwards, creating low-velocity streaks $-u'$, and *viceversa* (Landahl 1980; Brandt 2014; Jiménez 2018).

The above analysis is based on the linearized equations for streamwise-independent disturbances. Nonlinear effects can be considered in the resolvent framework, with nonlinear terms considered as forcing, as described in § 4.2. In this case, streamwise vortices (v' and w' velocity fluctuations) are excited by the f_y and f_z forcing terms in the y and z directions. For a turbulent flow, such a forcing corresponds to nonlinear terms in the momentum equations. Thus, nonlinearities in the turbulent flow cause the formation of streamwise vortices. Once such vortices are excited, they lead to the appearance of streaks via the lift-up effect, similar to the description of Ellingsen & Palm (1975). In what follows, the references to the lift-up effect should be understood in the context of such a forced problem, with nonlinearities that excite streamwise vortices.

Accordingly, the lift-up effect has been shown to arise also in the analysis of the linearized problem subject to forcing (Jovanović & Bamieh 2005), with optimal forcing dominated by y and z components shaped as a streamwise vortex (Hwang & Cossu 2010), creating v and w components in the flow, streamwise vortices that lead to highly amplified streaks of streamwise velocity. This effect plays an important role in the near-wall cycle described by Hamilton *et al.* (1995), Hall & Sherwin (2010) and Farrell & Ioannou (2012), with a self-sustained cycle where streamwise vortices generate streaks, which, once high amplitudes are attained, break down due to instabilities. Subsequent nonlinear interactions among streamwise oscillatory modes generated by streak instability lead to streamwise vortex regeneration, thus restarting the cycle. Due to the importance of lift-up to wall-bounded turbulent flows, we focus our analysis on the coherent structures involved in such mechanism, such as streaks and streamwise vortices.

4. Methodologies

4.1. *Spectral proper orthogonal decomposition*

In the present study, SPOD follows the procedure outlined by Towne *et al.* (2018). The method is applied to the velocity fluctuation components u', v' and w' to characterize the turbulent kinetic energy. We first apply a fast Fourier transform (FFT) to the velocity fields in the homogeneous directions x and z to obtain the field for specific wavenumbers k_x and m, respectively. We also perform a FFT to the velocity fields in time to obtain the field for a specific frequency ω, so $\hat{q} = \hat{q}(k_x, r, m, \omega)$, where hats denote Fourier-transformed quantities and $\hat{q} = [\hat{u}; \hat{v}; \hat{w}]$ are the state variables; we then apply the SPOD to this transformed field, which is equivalent to solving the integral equation

$$\int_{r'} \boldsymbol{C}(r, r', \omega)\boldsymbol{\Psi}(r', \omega)r' \, \mathrm{d}r' = \lambda(\omega)\boldsymbol{\Psi}(r, \omega), \tag{4.1}$$

where $\boldsymbol{\Psi}$ are basis functions, or SPOD modes, λ is the corresponding eigenvalue and $\boldsymbol{C}$ is the two-point cross-spectral density between the three velocity components, whose dimension is $3N_r x 3N_r$, where N_r is the number of points in the radial coordinates. Note that $\boldsymbol{C}$ is Hermitian, and thus eigenvalues are real and eigenfunctions are orthogonal. The decreasing ordering of the eigenvalues ensures that the most energetic modes in terms of kinetic energy are the first ones.

Since the number of grid points is high, we use the snapshot method, originally introduced by Sirovich (1987), which is more effective in computing the SPOD numerically, as presented by Towne *et al.* (2018) and Schmidt & Colonius (2020).

The short-time fast Fourier transform required to solve the SPOD was taken considering blocks containing 32 snapshots with 75 % overlap, which leads to 22 and 29 blocks for $Re_\tau = 180$ and 550, respectively. Spectral proper orthogonal decomposition was also evaluated using blocks containing 48 snapshots with 50 % and 75 % of overlap, and the changes in the results were not significant. Changes in leading eigenvalues did not exceed 0.1 % in most of the frequency/wavenumber combinations, indicating that the SPOD results are reliable and can be meaningfully analysed.

In order to further verify the reliability of the computed SPOD modes, we carry out a convergence analysis, by dividing the total dataset into two equal parts each corresponding to 75 % of the original dataset, and performing the SPOD on each part, so a normalized inner product is given by

$$\mu_{i,k} = \frac{\langle \boldsymbol{\Psi}_k, \boldsymbol{\Psi}_{i,k} \rangle}{\|\boldsymbol{\Psi}_k\| \cdot \|\boldsymbol{\Psi}_{i,k}\|}, \tag{4.2}$$

where $\langle , \rangle$ denotes the standard L_2 inner product considering the three velocity components, $i = (1; 2)$ indicates each subset and k each SPOD mode. This kind of analysis was also performed by Lesshafft *et al.* (2019) and Abreu, Cavalieri & Wolf (2017). Figures 5(*a*) and 5(*b*) show the normalized inner products of (4.2) considering $(\lambda_x^+, \lambda_z^+, \lambda_t^+) \approx (1000, 100, 100)$ for $Re_\tau = 180$ and 550, respectively. Results show that the less energetic SPOD modes show discrepancies, which can be explained by the differences in the order in which the modes appear on each subset. However, for $Re_\tau = 180$ we can observe that the first three SPOD modes exhibit a correlation coefficient close to one and can be considered as converged, and for $Re_\tau = 550$ the first two modes are reasonably converged.

The convergence analysis of the SPOD modes is sensitive to the amount of data used (Lesshafft *et al.* 2019). The DNS databases analysed here contain a limited number of
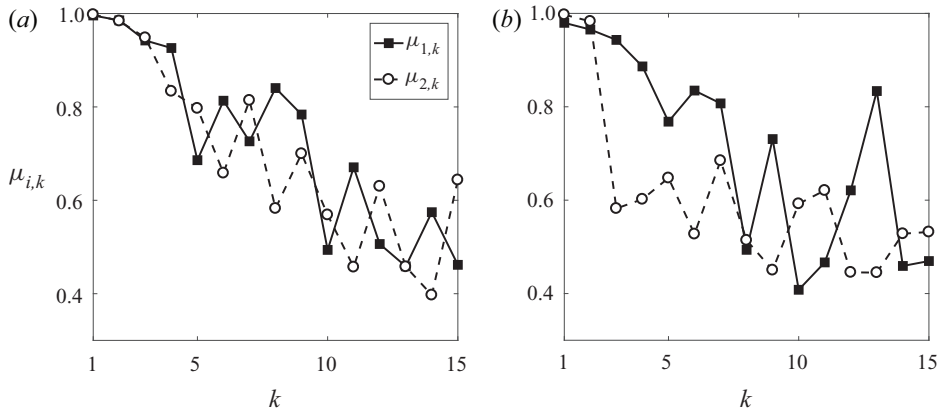
FIGURE 5. Correlation coefficient $\mu_{i,k}$ to quantify the statistical convergence of the SPOD modes, considering $(\lambda_x^+, \lambda_z^+, \lambda_t^+) \approx (1000, 100, 100)$ for both Reynolds numbers: (*a*) $Re_\tau = 180$; (*b*) $Re_\tau = 550$.

snapshots, but for all analysed cases of $(\lambda_x^+, \lambda_z^+, \lambda_t^+)$ studied in this paper, the first two SPOD modes were found to be converged for both Reynolds numbers, with $\mu_{i,k} \geq 0.95$.

4.2. *Resolvent analysis*

To perform the resolvent analysis we follow the formulation described by McKeon & Sharma (2010), also for a turbulent pipe flow. The linearized Navier–Stokes system for fully developed incompressible pipe flow can be written in operator notation as

$$\hat{q} = C(i\omega I - L)^{-1} B \hat{f}, \tag{4.3}$$

where L is the linearized Navier–Stokes operator considering the mean profile $\bar{u}$ (averaged in time, streamwise and azimuthal coordinates) as a base flow, ω is the analysed frequency, $\hat{q} = [\hat{u}; \hat{v}; \hat{w}]$ is a vector containing all velocity components, $\hat{f} = [\hat{f}_x; \hat{f}_y; \hat{f}_z]$, or nonlinear terms from Navier–Stokes equations, in streamwise, wall-normal and azimuthal directions and finally the linear operators B and C are filters that impose restrictions both the forcing and in the output quantities of interest, respectively. Note that B guarantees that no force will be applied in the continuity equation, and C amounts to observation of only velocity fluctuations. The input is thus taken as the forcing term in the momentum equation, interpreted as the nonlinear terms not considered in the linearization of the Navier–Stokes equation, also labelled as generalized Reynolds stresses (for a given frequency/wavenumber combination). The output is based on a norm involving solely velocity fluctuations, and its maximization of the output thus leads to maximal turbulent kinetic energy. The linearized Navier–Stokes operator here involves only the molecular viscosity, as in McKeon & Sharma (2010). Even though it has been shown in some works that inclusion of an eddy viscosity improves the agreement between resolvent modes and flow statistics (Morra *et al.* 2019; Pickering *et al.* 2020), the present choice is motivated by a more straightforward interpretation of the forcing f as the nonlinear terms; more detailed analysis of such forcing terms are currently being carried out by our group in related works (Nogueira *et al.* 2020). All variables here are Fourier transformed in time, streamwise and azimuthal directions.

It should be pointed out that the choice of base flow is not unique. A number of works (e.g. Waleffe 1997; Schoppa & Hussain 2002; Farrell & Ioannou 2012) carry out analysis using a base flow resulting from averaging on the streamwise direction. The resulting flow is x- and t-dependent, and may be subject to streak instability and transient growth. In this work, we have chosen to use the mean flow with averaging in all homogeneous directions. This facilitates comparison with SPOD modes taken from data, as such modes display better statistical convergence once preliminary Fourier decompositions are applied to the database. This allows a broad comparison between resolvent modes and DNS data, with the caveat that mechanisms such as streak instability and transient growth cannot be detected in the analysis in straightforward manner.

The resolvent operator is defined as $\boldsymbol{R} = \boldsymbol{C}(i\omega\boldsymbol{I} - \boldsymbol{L})^{-1}\boldsymbol{B}$, and its singular value decomposition leads to optimal forcing modes, causing maximum amplification between input and output,

$$\boldsymbol{R} = \boldsymbol{U}\boldsymbol{\Sigma}\boldsymbol{V}^{\dagger}, \tag{4.4}$$

where $\dagger$ superscript indicates the Hermitian of the matrix. The above equation decomposes $\boldsymbol{R}$ into two orthonormal bases $\boldsymbol{U}$ and $\boldsymbol{V}$, where $\boldsymbol{U}^{\dagger}\boldsymbol{U} = \boldsymbol{I}$ and $\boldsymbol{V}^{\dagger}\boldsymbol{V} = \boldsymbol{I}$. Here $\boldsymbol{U}$ is the output and $\boldsymbol{V}$ is the input bases, so the size of $\boldsymbol{U}$ is $N_q \times N_{modes}$ and the size of $\boldsymbol{V}$ is $N_f \times N_{modes}$, where N_q is the size of the output $\hat{q}$, N_f if the size of the input $\hat{f}$ and N_{modes} is the number of resolvent modes. The matrix $\boldsymbol{\Sigma}$ is diagonal, with real, positive values, in decreasing order $\sigma_1 \geq \sigma_2 \geq \cdots \geq \sigma_n$.

This approach leads to identification of modes that optimally describe the linear amplification mechanisms in stable systems. In particular, resolvent analysis evaluates the flow response to time-periodic forcing. The method provides two orthonormal bases, one for forcing and the other one for the associated flow responses, and each pair of forcing and response modes is related by a gain. Response modes with high gains are expected to be dominant in the flow, as will be described next. Here we investigate how the response modes obtained using resolvent analysis are able to model dominant structures in turbulent pipe flow, which can be extracted from the DNS database. More details about the present resolvent formulation can be seen in McKeon & Sharma (2010), and the relationship between SPOD and resolvent modes is documented in Towne *et al.* (2018) and Lesshafft *et al.* (2019).

The mean velocity profiles used to compute the resolvent analysis, $\bar{u} = \bar{u}(1 - r)$, were extracted from the simulation considering azimuthal, streamwise and temporal averages. The base flow in wall units is shown in figure 2(a) for both Reynolds numbers.

4.3. *SPOD versus resolvent analysis*

Recent works have explored the connection between SPOD modes and the flow responses to stochastic forcing successfully (Abreu *et al.* 2017; Towne *et al.* 2018; Lesshafft *et al.* 2019). To relate mathematically SPOD and resolvent analysis we can write the relation between the flow realizations $\hat{q}$ and the resolvent operator $\boldsymbol{R}$ for a problem with harmonic forcing $\hat{f}$ as

$$\hat{q} = \boldsymbol{R}\hat{f}. \tag{4.5}$$

Analysis of stochastic fields require a formulation in terms of two-point statistics. This can be obtained by multiplying (4.5) by its Hermitian and taking the expected value $\mathcal{E}()$ of

the forcing. This leads to

$$\mathcal{E}(\hat{q}\hat{q}^{\dagger}) = \boldsymbol{R}\mathcal{E}(\hat{f}\hat{f}^{\dagger})\boldsymbol{R}^{\dagger}. \tag{4.6}$$

If the forcing is white noise in space, $\mathcal{E}(\hat{f}\hat{f}^{\dagger}) = \boldsymbol{I}$, (4.6) becomes

$$\boldsymbol{\psi}\boldsymbol{\Lambda}\boldsymbol{\Psi}^{\dagger} = \boldsymbol{U}\boldsymbol{\Sigma}^2\boldsymbol{U}^{\dagger}, \tag{4.7}$$

meaning that the SPOD modes are simply the response modes from resolvent analysis, with SPOD eigenvalues equal to the square of resolvent gains.

It is clear that the forcing is not white noise in space, as, for instance, nonlinear terms in the Navier–Stokes system vanish on the wall. The analysis of Nogueira *et al.* (2020) for a minimal flow unit suggests that the forcing statistics are spatially coherent. In this case, the response statistics depend on the details of the forcing in (4.6), such that

$$\boldsymbol{\psi}\boldsymbol{\Lambda}\boldsymbol{\psi}^{\dagger} = \boldsymbol{U}\boldsymbol{\Sigma}\boldsymbol{V}^{\dagger}\boldsymbol{E}(\hat{f}\hat{f}^{\dagger})\boldsymbol{V}\boldsymbol{\Sigma}\boldsymbol{U}^{\dagger}. \tag{4.8}$$

However, if the resolvent operator has a dominant amplification mechanism, such that $\sigma_1 \ll \sigma_2$, the response CSD will be dominated by the contribution of the leading response mode (Beneddine *et al.* 2016; Towne *et al.* 2018; Cavalieri *et al.* 2019). To see this, neglecting the high-order gains leads to

$$\mathcal{E}(\hat{q}\hat{q}^{\dagger}) \approx \boldsymbol{u}_1\boldsymbol{\sigma}_1\boldsymbol{v}_1^{\dagger}\mathcal{E}(\hat{f}\hat{f}^{\dagger})\boldsymbol{v}_1\boldsymbol{\sigma}_1\boldsymbol{u}_1^{\dagger} \tag{4.9}$$

and hence the flow response is approximately given by the projection of the forcing statistics onto the optimal forcing mode $\boldsymbol{v}_1$, amplified by the leading gain $\boldsymbol{\sigma}_1$ and taking the shape of the most amplified response $\boldsymbol{u}_1$. In this case the leading SPOD mode may be close to the optimal flow response, even though the forcing is not white in space.

The expressions above consider a Euclidean inner product, which is appropriate for matrices. The non-uniform grids used in this work require the use of integration weights for the discretization of the inner product. Resolvent analysis and SPOD should be modified so as to account for integration weights; appropriate expressions are presented by Towne *et al.* (2018), Lesshafft *et al.* (2019) and Cavalieri *et al.* (2019) and are not repeated here for brevity.

5. Results and discussions

Figures 6 and 7 show the first two SPOD modes compared with the optimal and suboptimal responses from resolvent analysis for $Re_\tau = 180$ and 550, respectively, considering $(\lambda_x^+, \lambda_z^+, \lambda_t^+) \approx (1000, 100, 100)$, or the corresponding frequency $\omega^+ = 2\pi/\lambda_t^+ \approx 0.06$. This is representative of the near-wall cycle, corresponding to the peak wavenumber in the premultiplied spectra shown in figure 4 and to a phase speed of $c^+ \approx 10$, a value typical of buffer-layer disturbances. Notice that the vertical direction does not correspond to constant spacing in viscous length scale, due to polar system. The results for the first mode for both Reynolds numbers (figures 6*a,b* and 7*a,b*) show that the velocity field is associated with streamwise vortices (shown with arrows) and accompanying low- and high-speed streaks (colours). Negative wall-normal fluctuations carry high-momentum fluid and create high-velocity streaks with $u' > 0$ (red contour lines), and the opposite occurs for the positive wall-normal disturbances, creating slow-velocity streaks with $u' < 0$ (blue contour lines), characterizing the lift-up mechanism (Hwang & Cossu 2010; Brandt 2014). The second mode (figures 6*c,d*
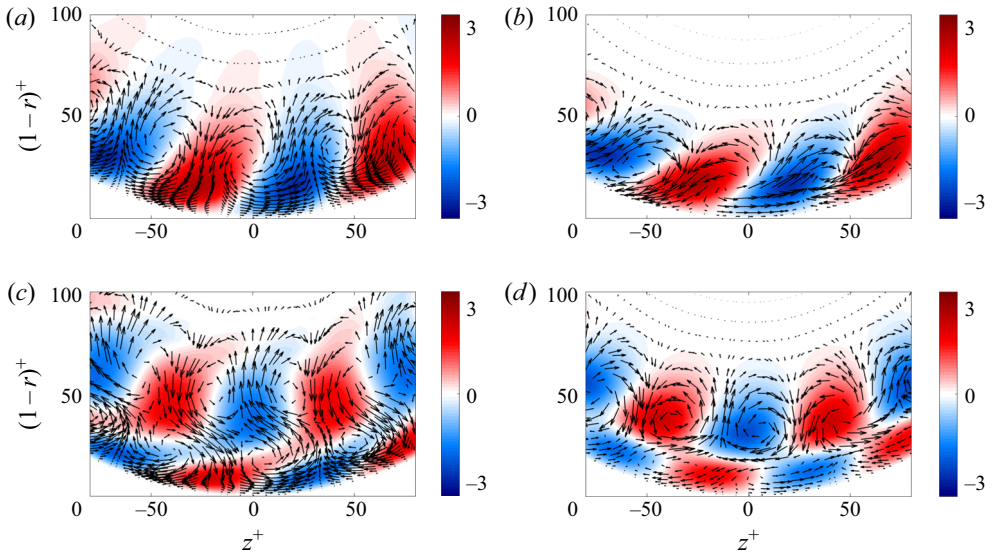
FIGURE 6. Comparison between the first two SPOD modes and optimal and suboptimal responses from resolvent analysis using cross-stream view of the $v - w$ components of the vortices (arrows) and the u component of the streak (red and blue contours) for $(\lambda_x^+, \lambda_z^+, \lambda_t^+) \approx$ (1000, 100, 100) at $Re_\tau = 180$. The axis ticks labels are scaled in inner units. (*a*) SPOD mode 1; (*b*) resolvent mode 1; (*c*) SPOD mode 2; (*d*) resolvent mode 2.
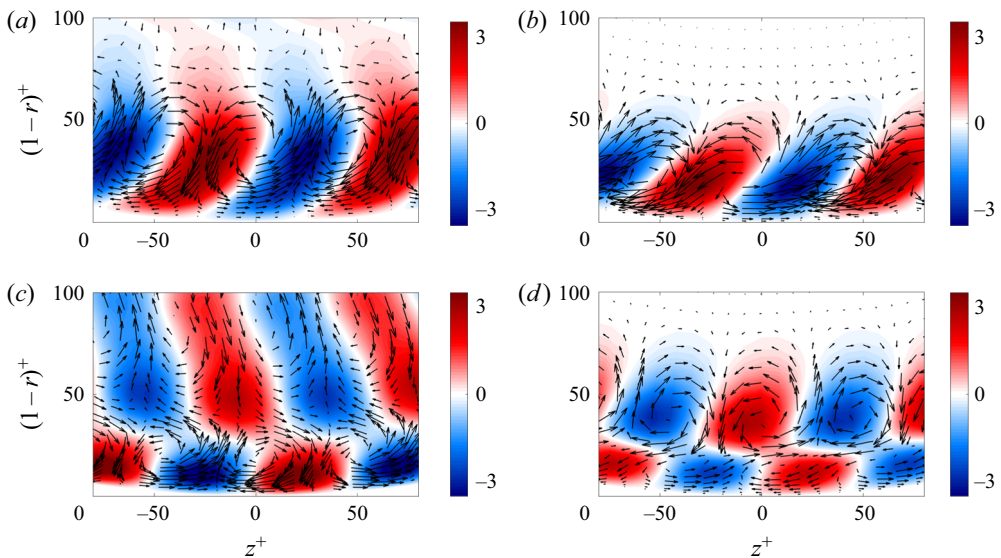

FIGURE 7. Comparison between the first two SPOD modes and optimal and suboptimal responses from resolvent analysis using cross-stream view of the $v - w$ components of the vortices (arrows) and the u component of the streak (red and blue contours) for $(\lambda_x^+, \lambda_z^+, \lambda_t^+) \approx$ (1000, 100, 100) at $Re_\tau = 550$. The axis ticks labels are scaled in inner units. (*a*) SPOD mode 1; (*b*) resolvent mode 1; (*c*) SPOD mode 2; (*d*) resolvent mode 2.

and 7*c*,*d*) shows a pattern with two streamwise vortices and two streaks as a function of radius, similar to the observations of Hellström *et al.* (2016) for higher-order POD modes of larger-scale structures at higher Reynolds number. Streamwise vortices and streaks are again arranged consistently with the lift-up mechanism. The results show that the optimal and suboptimal flow responses recover the leading SPOD modes for both Reynolds numbers, highlighting that the responses obtained using the linearized operator serve as a pertinent model for the dominant structures observed in the DNS for the analysed frequency/wavenumber combination, $(\lambda_x^+, \lambda_z^+, \lambda_t^+) \approx (1000, 100, 100)$.

Our aim is to perform additional, detailed quantitative comparisons between the first SPOD mode from the DNS and the optimal response from resolvent analysis. In order to evaluate the agreement for several values of wavelengths λ_x and λ_z at a fixed frequency ω, we define the metric

$$\beta = \frac{\langle \hat{\boldsymbol{q}}_{1\mathrm{SPOD}}, \hat{\boldsymbol{q}}_{1\mathrm{RES}} \rangle}{\|\hat{\boldsymbol{q}}_{1\mathrm{SPOD}}\| \cdot \|\hat{\boldsymbol{q}}_{1\mathrm{RES}}\|}, \tag{5.1}$$

where $\hat{\boldsymbol{q}}_{1\mathrm{SPOD}} = [\hat{\boldsymbol{u}}_{1\mathrm{SPOD}}, \hat{\boldsymbol{v}}_{1\mathrm{SPOD}}, \hat{\boldsymbol{w}}_{1\mathrm{SPOD}}]$ is the first SPOD mode, $\hat{\boldsymbol{q}}_{1\mathrm{RES}} = [\hat{\boldsymbol{u}}_{1\mathrm{RES}}, \hat{\boldsymbol{v}}_{1\mathrm{RES}}, \hat{\boldsymbol{w}}_{1\mathrm{RES}}]$ is the optimal response from resolvent analysis and β is the projection of $\hat{\boldsymbol{q}}_{1\mathrm{SPOD}}$ into $\hat{\boldsymbol{q}}_{1\mathrm{RES}}$ (note that $\langle \cdot, \cdot \rangle$ denotes the L_2 inner product). Thus, $\beta = 1$ indicates a perfect alignment between both vectors and $\beta = 0$ indicates that the modes are orthogonal. The SPOD and resolvent modes include all velocity components in order to include information about the phase.

Results of agreement between the first SPOD mode and the optimal response from resolvent analysis in terms of β are shown in figure 8(*a–c*) for $Re_\tau = 180$ at fixed frequencies corresponding to $\lambda_t^+ \approx 100, 250$ and 1500; and in figure 9(*a–c*) for $Re_\tau = 550$ at $\lambda_t^+ \approx 100, 250$ and 1000. The frequencies are discretized by the application of the Welch method, and were chosen to be representative of the near-wall cycle ($\lambda_t^+ \approx 100$) and of lower frequencies of larger structures. The red dashed line in all plots in figures 8 and 9 represents the line $\lambda_x^+ = 2\lambda_z^+$, such that below that line the structures are elongated in the streamwise direction with $\lambda_x^+ > 2\lambda_z^+$. The black dashed line represents $\lambda_x^+ = U_{max}^+ \lambda_t^+$, representing the limit where the phase velocity c^+ is equal to the velocity in the pipe centre U_{max}^+. Results show for both Reynolds numbers that the coefficient β is close to one for a large part of the parameter space, highlighting a significant region with very good agreement between the first SPOD and resolvent modes, most of it below the line $\lambda_x^+ = 2\lambda_z^+$, indicating that resolvent analysis leads to an accurate modelling of such turbulent structures in turbulent pipe flow for all the analysed frequencies.

In order to explore features leading to better or worse agreement, $\beta \approx 1$ or $\beta \approx 0$, respectively, we evaluated for both friction Reynolds numbers the ratio between optimal and suboptimal resolvent gains in logarithmic scale $\log_{10}(\sigma_1/\sigma_2)$, indicating regions where the optimal gain is much larger than the suboptimal; these results are shown in figure 8(*g–i*) for $Re_\tau = 180$ and figure 9(*g–i*) for $Re_\tau = 550$, for the considered frequencies in the preceding plots. We observe in general that regions where the first resolvent gain is much larger than the second correspond to the region of good SPOD–resolvent agreement, i.e. the triangular region below the red line $\lambda_x^+ = 2\lambda_z^+$ and to the left of the vertical line marking $c^+ = U_{max}^+$. This behaviour is observed even for some regions crossing the red line, for $\lambda_x^+ < 2\lambda_z^+$. This thus indicates that regions where the optimal response is much more dominant than the suboptimal may be accurately modelled considering the first SPOD mode. In this region the leading flow response predicted by resolvent analysis is much more amplified than suboptimal modes, which explains the agreement with leading modes from the DNS, as discussed in §4.3. The region at the right of the vertical lines
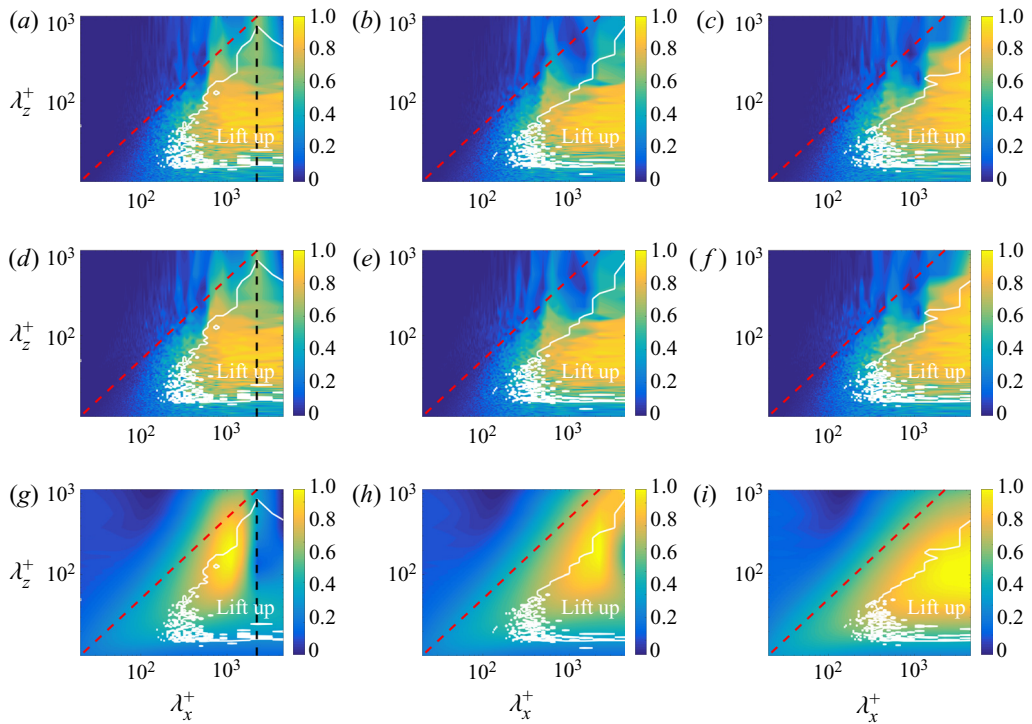
FIGURE 8. (*a–c*) Agreement between first SPOD mode and optimal response from resolvent analysis characterized in terms of β. (*d–f*) Agreement between first SPOD and resolvent modes considering $f_x = 0$, characterized in terms of $\beta_{(f_x=0)}$. (*g–i*) Ratio between optimal and suboptimal resolvent gains in logarithmic scale. Results for $Re_\tau = 180$ and fixed frequencies: $\lambda_t^+ \approx 100$, 250 and 1500 (from left to right). The region surrounded by the white line in all plots represents an indicator of lift-up mechanism from resolvent analysis. The red dashed line in all plots represents $\lambda_x^+ = 2\lambda_z^+$. (*a*) β, $\lambda_t^+ \approx 100$; (*b*) β, $\lambda_t^+ \approx 250$; (*c*) β, $\lambda_t^+ \approx 1500$; (*d*) $\beta_{(f_x=0)}$, $\lambda_t^+ \approx 100$; (*e*) $\beta_{(f_x=0)}$, $\lambda_t^+ \approx 250$; (*f*) $\beta_{(f_x=0)}$, $\lambda_t^+ \approx 1500$; (*g*) $\log_{10}(\sigma_1/\sigma_2)$, $\lambda_t^+ \approx 100$; (*h*) $\log_{10}(\sigma_1/\sigma_2)$, $\lambda_t^+ \approx 250$; (*i*) $\log_{10}(\sigma_1/\sigma_2)$, $\lambda_t^+ \approx 1500$.

in the plots has low dominance of the leading resolvent mode, as shown in figures 8(*g–i*) and 9(*g–i*), but nonetheless displays good agreement with SPOD modes. The said regions are seen to lie to the right of the vertical line marking a phase speed equal to the mean velocity at the jet centreline. Such frequency and wavenumber combinations thus relate to disturbances with phase speed higher than the mean velocity anywhere in the pipe, and are therefore not of much interest.

The analysis above highlights that a better agreement between leading SPOD and resolvent modes is observed when a certain mode dominance is verified by analysis of the linearized operator. We now investigate whether this dominance can be attributed to the lift-up mechanism, understood in the present turbulent regime as transverse forcing components (nonlinear terms in the radial and azimuthal momentum equations) giving rise to streamwise vortices, which in turn lead to high-amplitude streaks, as discussed in §3. The region delimited by the white line in figures 8 and 9 denotes the presence of the lift-up effect, purely from the resolvent analysis, at $Re_\tau = 180$ and 550, respectively. This region shows an indicator of lift-up mechanism, which is here considered to be relevant when the ratio of peak transverse and streamwise forcings, $\max(|f_y|/|f_x|)$ and $\max(|f_z|/|f_x|)$
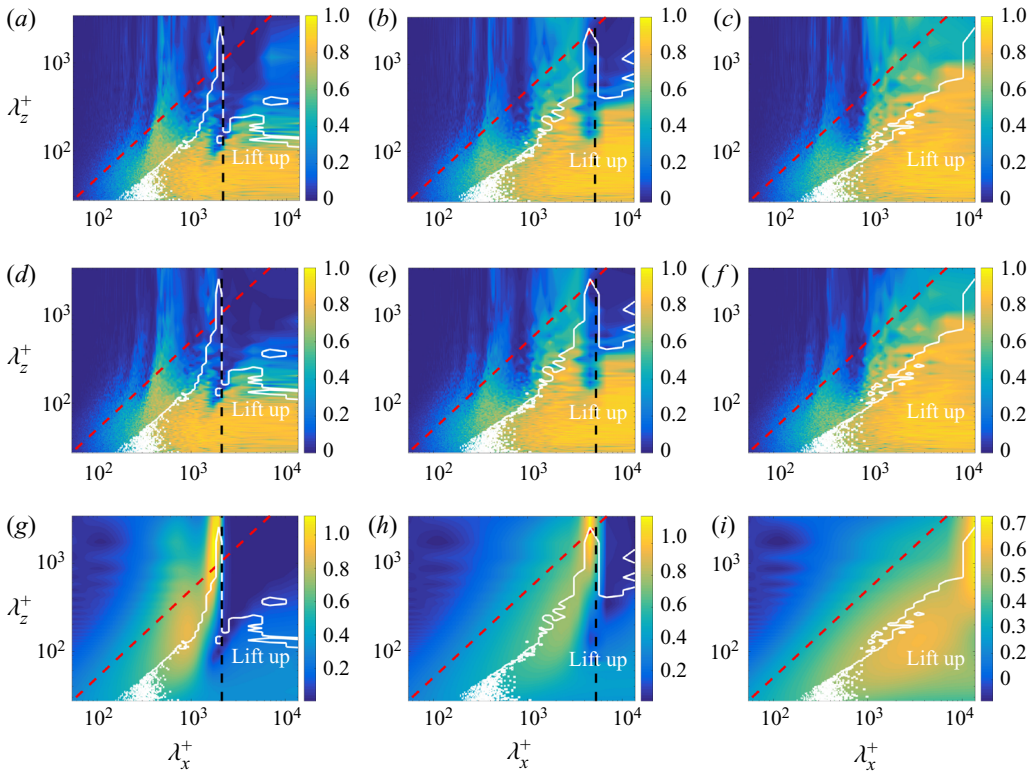
FIGURE 9. (*a–c*) Agreement between first SPOD mode and optimal response from resolvent analysis characterized in terms of β. (*d–f*) Agreement between first SPOD and resolvent modes considering $f_x = 0$, characterized in terms of $\beta_{(f_x=0)}$. (*g–i*) Ratio between optimal and suboptimal resolvent gains in logarithmic scale. Results for $Re_\tau = 550$ and fixed frequencies: $\lambda_t^+ \approx 100$, 250 and 1000 (from left to right). The region surrounded by the white line in all plots represents an indicator of lift-up mechanism from resolvent analysis. The red dashed line in all plots represents $\lambda_x^+ = 2\lambda_z^+$. (*a*) β, $\lambda_t^+ \approx 100$; (*b*) β, $\lambda_t^+ \approx 250$; (*c*) β, $\lambda_t^+ \approx 1000$; (*d*) $\beta_{(f_x=0)}$, $\lambda_t^+ \approx 100$; (*e*) $\beta_{(f_x=0)}$, $\lambda_t^+ \approx 250$; (*f*) $\beta_{(f_x=0)}$, $\lambda_t^+ \approx 1500$; (*g*) $\log_{10}(\sigma_1/\sigma_2)$, $\lambda_t^+ \approx 100$; (*h*) $\log_{10}(\sigma_1/\sigma_2)$, $\lambda_t^+ \approx 250$; (*i*) $\log_{10}(\sigma_1/\sigma_2)$, $\lambda_t^+ \approx 1000$.

(indicating streamwise vortices as optimal forcing) and the ratio of peak transverse and streamwise velocity components, $\max(|u|/|v|)$ and $\max(|u|/|w|)$ (indicating streaks of streamwise velocity as associated most amplified response) are simultaneously larger than one. The regions satisfying these criteria are inside the 'lift-up' contour, or the white line, in figures 8 and 9. The result shows that the regions where the lift-up mechanism is present are close to those where β is around one, and also to parameters with dominance of the optimal forcing in resolvent analysis. The present results highlight that the lift-up mechanism is active for a wide range of frequencies and wavenumbers in turbulent pipe flow for both Reynolds numbers analysed here, with a strong amplification mechanism leading to structures that dominate the near-wall velocity field.

To further explore the lift-up effect, we performed the resolvent analysis neglecting the forcing in the streamwise direction (restricting $f_x = 0$ using the $\mathcal{B}$ operator), which should retain the lift-up mechanism, as the streamwise forcing f_x is not expected to be relevant in this case. We evaluated the agreement between the first SPOD and resolvent
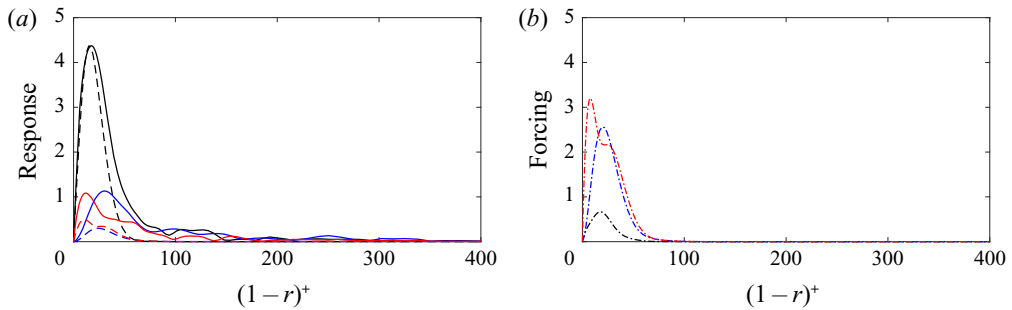
FIGURE 10. Case of $\beta = 0.95$ for $Re_\tau = 550$ and combination $(\lambda_x^+, \lambda_z^+, \lambda_t^+) \approx$ (1000, 100, 100), showing in panel (*a*) the comparison between first SPOD mode and the optimal response from resolvent analysis for the three velocity components and in panel (*b*) the associated forcing from resolvent analysis for the three components (f_x, f_y, f_z).

mode for this case, denoted as $\beta_{(f_x=0)}$. Results are shown in figures 8(*d–f*) and 9(*d–f*) for $Re_\tau = 180$ and 550, respectively. Similar agreement between SPOD and resolvent modes is obtained, despite the fact that the streamwise forcing was neglected. Parameters where good agreement is found also correspond to the region surrounded by the white line, defined by the lift-up indicator. Such results confirm that in the roughly triangular region, marking streamwise elongated structures with phase speeds lower than the centreline velocity, the lift-up mechanism is dominant, with transverse forcing components leading to streamwise vortices that in turn create amplified streaks. The relevance of such mechanism in resolvent analysis is seen by a large gain ratio, $\sigma_1 \ll \sigma_2$, and the dominance of the optimal response leads to good agreement with the leading SPOD mode from the DNS.

To see some sample results of the above analysis in more detail, figure 10 shows for $Re_\tau = 550$ results of comparisons between SPOD and resolvent modes for the combination $(\lambda_x^+, \lambda_z^+, \lambda_t^+) \approx (1000, 100, 100)$, which is representative of the signature of the near-wall cycle of streaks and streamwise vortices, with $\beta = 0.95$. In contrast, figure 11 shows the same kind of comparison, but for a larger azimuthal wavelength $(\lambda_x^+, \lambda_z^+, \lambda_t^+) \approx$ (1000, 500, 100), which leads to a $\beta = 0.11$ and thus substantial discrepancies between SPOD and resolvent modes. Figures 10(*a*) and 11(*a*) show the first SPOD mode compared with the optimal response from resolvent analysis for the three velocity components (u, v, w), for the cases with $\beta = 0.95$ and $\beta = 0.11$, respectively. We can see that the resolvent analysis reproduces very well the coherent structures obtained using SPOD for the case $(\lambda_x^+, \lambda_z^+, \lambda_t^+) \approx (1000, 100, 100)$, which has a large ratio $\lambda_x^+/\lambda_z^+ = 10$, indicative of very elongated streaky structures. The agreement is better for the streamwise component u, while the v and w components have similar shapes in the resolvent and SPOD modes, but have larger amplitudes in the case of the SPOD. This indicates that the streaks are reproduced well, whereas the in-plane velocities responsible for the streamwise vortices are underpredicted by a factor of around three. The phases between velocity components are nonetheless matched, as shown in figure 7; otherwise, a lower agreement metric would be obtained. On the other hand, the optimal response from the resolvent is not able to model the structure for the case $(\lambda_x^+, \lambda_z^+, \lambda_t^+) \approx (1000, 500, 100)$; here, the ratio $\lambda_x^+/\lambda_z^+ \approx 2$ is much lower, departing from the streaky disturbances typical of the lift-up mechanism. In particular, the spanwise wavelength of $\lambda_z^+ = 500$ implies that these structures are centred farther from the wall. This is evident from the fact that the SPOD modes exhibit significant energy in the range from $(1 - r)^+ = 200$ to around 400. On the other hand, but as in the case with $\beta = 0.95$, the resolvent modes exhibit high energy
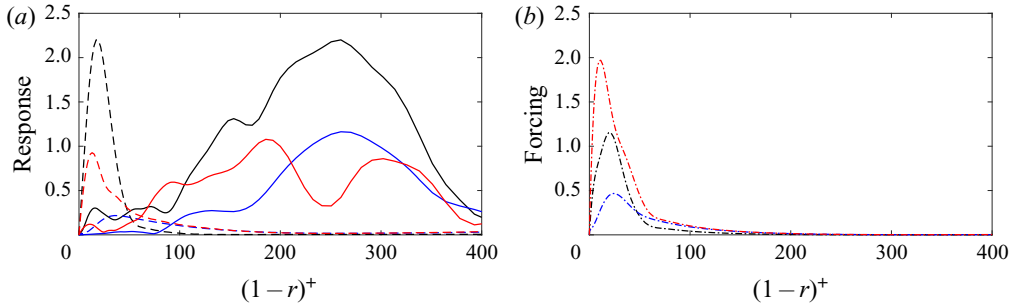
FIGURE 11. Case of $\beta = 0.11$ for $Re_\tau = 550$ and combination $(\lambda_x^+, \lambda_z^+, \lambda_t^+) \approx$ $(1000, 500, 100)$, showing in panel (*a*) the comparison between first SPOD mode and the optimal response from resolvent analysis for the three velocity components and in panel (*b*) the associated forcing from resolvent analysis for the three components (f_x, f_y, f_z).

mainly in the near-wall region, and are therefore unable to reproduce the flow dynamics in this case.

Figures 10(*b*) and 11(*b*) show the forcing from resolvent analysis for the three components (f_x, f_y, f_z), in the cases with $\beta = 0.95$ and $\beta = 0.11$, respectively. We can notice that when $\beta \approx 1$ the forcing corresponds to streamwise vortices, since f_y and f_z are simultaneously larger than f_x. On the other hand, when $\beta \approx 0$ the forcing can no longer be associated with such streamwise vortices, since here f_x becomes much larger than f_y. These results indicate that the lift-up mechanism is not present in that case, and thus reinforce the conclusion that resolvent analysis is an adequate reduced-order model to reproduce streaky structures associated with the lift-up mechanism. The observed concordances were generally for structures with peak in the buffer layer for both Reynolds numbers.

6. Conclusions

In the present study we used signal processing of a DNS, based on SPOD, to identify near-wall coherent structures in a turbulent pipe flow for friction Reynolds numbers $Re_\tau = 180$ and 550. In order to model such structures, a theoretical approach, i.e. resolvent analysis, was used. The homogeneous directions of this flow allow the evaluation of SPOD and resolvent analysis over a range of streamwise and azimuthal wavenumbers and frequencies. The mean flow was used as a basis for the computation of resolvent modes; optimal responses were considered as the most likely structures to be excited by nonlinear terms in the Navier–Stokes system, particularly when the gain of the optimal forcing is much larger than for suboptimal ones (Beneddine *et al.* 2016; Cavalieri *et al.* 2019). Coherent structures in the flow were extracted using SPOD, and we carried out thorough quantitative comparisons between leading response modes from the resolvent analysis and the SPOD eigenfunctions.

For both Reynolds numbers, the results show good agreement between SPOD and resolvent, mostly for $\lambda_x^+ \geq 2\lambda_z^+$. These are parameters related to streaky structures, with aspect ratio (streamwise over azimuthal extent) larger than two. We evaluated the ratio between the first and second SPOD eigenvalues, as well the ratio between the optimal and suboptimal gain from resolvent analysis, and observed that the regions where those ratios have larger values correspond to cases where the agreement between SPOD and resolvent modes are good.

We also explored the physical reasons behind this agreement by introducing an indicator of the lift-up mechanism using the optimal forcing and associated response from resolvent analysis. In the present turbulent flow, such a mechanism is considered as active when the forcing is related to wall-normal and azimuthal components, and the associated responses to streaks. In this case, nonlinearities excite streamwise vortices, which in turn lead to high-amplitude streaks (Hwang & Cossu 2010; Brandt 2014). The results show a clear lift-up effect for wavenumbers and frequencies with good agreement between SPOD and resolvent modes. Also, the observed concordances were generally for structures with peaks in the buffer layer.

In conclusion, based on our results, it can be stated that the resolvent analysis provides a simplified model leading to an accurate representation of coherent structures mostly for the cases where the lift-up mechanism is present, with the optimal forcing corresponding to transverse components shaped as streamwise vortices, and the associated response corresponding to streaks. Such structures are observed for a broad range of frequencies and wavenumbers, which indicates that the lift-up effect occurs over a wide range of scales in turbulent pipe flow. Earlier studies in turbulent channel flow have applied transient growth (Del Alamo & Jimenez 2006) and resolvent analysis (McKeon & Sharma 2010), extracting structures consistent with observations from simulation and experiment. Here, the analysis is made for a broad range of scales, showing the relevance of lift-up for the studied structures and highlighting the pertinence of linearized models.

It is not surprising to find streamwise vortices leading to streaks in wall-bounded turbulence, since this has been considered as an important part of the dynamics of such flows for some time (Kline *et al.* 1967; Landahl 1980; Hamilton *et al.* 1995). The present results highlight the relevance of this mechanism for most of the parameters considered in turbulent pipe flow, which can be understood by the clear dominance of the optimal forcing, with the shape of streamwise vortices, in leading to amplified flow responses of streaky shape. Lift-up thus is naturally selected as the preferred mechanism giving rise to streaky structures in turbulent pipe flow.

The use of resolvent analysis for such a wide range of turbulent scales is relevant. For parallel flows, in particular, the resolvent operator only needs to be discretized in the radial direction, and forcing and response modes can be obtained in fast computations. This allows simple predictions of the dominant structures in turbulent flows. Moreover, reconstructions of flow fluctuations from a limited number of sensors are also possible using the resolvent operator (Towne *et al.* 2020), which opens possibilities for closed-loop control of turbulent flows. As the lift-up effect studied here is also the basis of bypass transition in boundary layers (Andersson, Berggren & Henningson 1999; Brandt 2014), extension of control methods used in bypass transition (Sasaki *et al.* 2019) is a promising direction for the control of wall-bounded turbulence.

Acknowledgements

Declaration of interests

The authors report no conflict of interest.

REFERENCES

ABREU, L. I., CAVALIERI, A. V. G. & WOLF, W. R. 2017 Coherent hydrodynamic waves and trailing-edge noise. *AIAA Paper* 2017-3173. American Institute of Aeronautics and Astronautics.

ANDERSSON, P., BERGGREN, M. & HENNINGSON, D. 1999 Optimal disturbances and bypass transition in boundary layers. *Phys. Fluids* **11** (1), 134–150.

BENEDDINE, S., SIPP, D., ARNAULT, A., DANDOIS, J. & LESSHAFFT, L. 2016 Conditions for validity of mean flow stability analysis. *J. Fluid Mech.* **798**, 485–504.

BRANDT, L. 2014 The lift-up effect: the linear mechanism behind transition and turbulence in shear flows. *Eur. Mech.* B/*Fluids* **47**, 80–96.

CAVALIERI, A. V. G., JORDAN, P. & LESSHAFFT, L. 2019 Wave-packet models for jet dynamics and sound radiation. *Appl. Mech. Rev.* **71** (2), 020802.

DEL ALAMO, J. C. & JIMENEZ, J. 2006 Linear energy amplification in turbulent channels. *J. Fluid Mech.* **559**, 205–213.

EITEL-AMOR, G., ÖRLÜ, R. & SCHLATTER, P. 2014 Simulation and validation of a spatially evolving turbulent boundary layer up to $Re_\theta = 8300$. *Intl J. Heat Fluid Flow* **47**, 57–69.

EL KHOURY, G. K., SCHLATTER, P., NOORANI, A., FISCHER, P. F., BRETHOUWER, G. & JOHANSSON, A. V. 2013 Direct numerical simulation of turbulent pipe flow at moderately high Reynolds numbers. *Flow Turbul. Combust.* **91** (3), 475–495.

ELLINGSEN, T. & PALM, E. 1975 Stability of linear flow. *Phys. Fluids* **18** (4), 487–488.

FARRELL, B. F. & IOANNOU, P. J. 1993 Stochastic forcing of the linearized Navier–Stokes equations. *Phys. Fluids* A **5** (11), 2600–2609.

FARRELL, B. F. & IOANNOU, P. J. 2012 Dynamics of streamwise rolls and streaks in turbulent wall-bounded shear flow. *J. Fluid Mech.* **708**, 149–196.

FISCHER, P. F., LOTTES, J. W. & KERKEMEIER, S. G. 2008 Nek5000: Open Source Spectral Element CFD Solver. Available at: http://nek5000.mcs.anl.gov.

GUPTA, A. K., LAUFER, J. & KAPLAN, R. E. 1971 Spatial structure in the viscous sublayer. *J. Fluid Mech.* **50** (3), 493–512.

HALL, P. & SHERWIN, S. 2010 Streamwise vortices in shear flows: harbingers of transition and the skeleton of coherent structures. *J. Fluid Mech.* **661**, 178–205.

HAMILTON, J. M., KIM, J. & WALEFFE, F. 1995 Regeneration mechanisms of near-wall turbulence structures. *J. Fluid Mech.* **287**, 317–348.

HELLSTRÖM, L. H. O., MARUSIC, I. & SMITS, A. J. 2016 Self-similarity of the large-scale motions in turbulent pipe flow. *J. Fluid Mech.* **792**.

HOYAS, S. & JIMÉNEZ, J. 2006 Scaling of the velocity fluctuations in turbulent channels up to $Re_\tau = 2003$. *Phys. Fluids* **18** (1), 011702.

HUTCHINS, N. & MARUSIC, I. 2007 Evidence of very long meandering features in the logarithmic region of turbulent boundary layers. *J. Fluid Mech.* **579**, 1–28.

HWANG, Y. & COSSU, C. 2010 Linear non-normal energy amplification of harmonic and stochastic forcing in the turbulent channel flow. *J. Fluid Mech.* **664**, 51–73.

JIMÉNEZ, J. 2018 Coherent structures in wall-bounded turbulence. *J. Fluid Mech.* **842**.

JOVANOVIĆ, M. R. & BAMIEH, B. 2005 Componentwise energy amplification in channel flows. *J. Fluid Mech.* **534**, 145–183.

KLINE, S. J., REYNOLDS, W. C., SCHRAUB, F. A. & RUNSTADLER, P. W. 1967 The structure of turbulent boundary layers. *J. Fluid Mech.* **30** (4), 741–773.

LANDAHL, M. T. 1980 A note on an algebraic instability of inviscid parallel shear flows. *J. Fluid Mech.* **98** (2), 243–251.

LESSHAFFT, L., SEMERARO, O., JAUNET, V., CAVALIERI, A. V. G. & JORDAN, P. 2019 Resolvent-based modeling of coherent wave packets in a turbulent jet. *Phys. Rev. Fluids* **4** (6), 063901.

LUMLEY, J. L. 1967 The structure of inhomogeneous turbulent flows. In *Atmospheric Turbulence and Radio Wave Propagation* (ed. A. M. Yaglom & V. I. Tatarsky). Nauka.

LUMLEY, J. L. 1970 *Stochastic Tools in Turbulence*, Applied Mathematics and Mechanics, vol. 12. Academic.

MARUSIC, I., BAARS, W. J. & HUTCHINS, N. 2017 Scaling of the streamwise turbulence intensity in the context of inner-outer interactions in wall turbulence. *Phys. Rev. Fluids* **2** (10), 100502.

McKeon, B. J. & Sharma, A. S. 2010 A critical-layer framework for turbulent pipe flow. *J. Fluid Mech.* **658**, 336–382.

McKeon, B. J., Sharma, A. S. & Jacobi, I. 2013 Experimental manipulation of wall turbulence: a systems approach. *Phys. Fluids* **25** (3), 031301.

Monty, J. P., Hutchins, N., Ng, H. C. H., Marusic, I. & Chong, M. S. 2009 A comparison of turbulent pipe, channel and boundary layer flows. *J. Fluid Mech.* **632**, 431–442.

Morra, P., Sasaki, K., Hanifi, A., Cavalieri, A. V. G. & Henningson, D. 2019 A realizable data-driven approach to delay bypass transition with control theory. arXiv:1902.05049.

Nogueira, P. A. S., Morra, P., Martini, E., Cavalieri, A. V. G. & Henningson, D. S. 2020 Forcing statistics in resolvent analysis: application in minimal turbulent Couette flow. arXiv:2001.02576.

Picard, C. & Delville, J. 2000 Pressure velocity coupling in a subsonic round jet. *Int. J. Heat Fluid Flow* **21** (3), 359–364.

Pickering, E. M., Rigas, G., Sipp, D., Schmidt, O. T. & Colonius, T. 2020 Optimal eddy viscosity for resolvent-based models of coherent structures in turbulent jets. arXiv:2005.10964.

Sasaki, K., Morra, P., Cavalieri, A. V. G., Hanifi, A. & Henningson, D. 2019 On the role of actuation for the control of streaky structures in boundary layers. arXiv:1902.04923.

Schmidt, O. T. & Colonius, T. 2020 Guide to spectral proper orthogonal decomposition. *AIAA J.* **58** (3), 1023–1033.

Schoppa, W. & Hussain, F. 2002 Coherent structure generation in near-wall turbulence. *J. Fluid Mech.* **453**, 57–108.

Sirovich, L. 1987 Turbulence and the dynamics of coherent structures. I. Coherent structures. *Q. Appl. Maths* **45** (3), 561–571.

Smith, C. R. & Metzler, S. P. 1983 The characteristics of low-speed streaks in the near-wall region of a turbulent boundary layer. *J. Fluid Mech.* **129**, 27–54.

Smits, A. J., McKeon, B. J. & Marusic, I. 2011 High–Reynolds number wall turbulence. *Annu. Rev. Fluid Mech.* **43**, 353–375.

Towne, A., Lozano-Durán, A. & Yang, X. 2020 Resolvent-based estimation of space–time flow statistics. *J. Fluid Mech.* **883**.

Towne, A., Schmidt, O. T. & Colonius, T. 2018 Spectral proper orthogonal decomposition and its relationship to dynamic mode decomposition and resolvent analysis. *J. Fluid Mech.* **847**, 821–867.

Trefethen, L. N., Trefethen, A. E., Reddy, S. C. & Driscoll, T. A. 1993 Hydrodynamic stability without eigenvalues. *Science* **261** (5121), 578–584.

Waleffe, F. 1997 On a self-sustaining process in shear flows. *Phys. Fluids* **9** (4), 883–900.